Digest Journal of Nanomaterials and Biostructures

Dig. J. Nanomater. Bios. **2026**; 21(4): 53465
https://doi.org/10.31083/DJNB53465

Original Research

Comparative Evaluation of g-C_3N_4 and ZnO Nanorods as Photocatalysts for the Sunlight-Driven Degradation of Cationic and Anionic Dyes

Suneel[1], Sandeep Gupta[2], M Shaheer Akhtar[3,4,*], Haroon[5], Ahamad Imran[6], Ravindra Kumar Gupta[6], Qazi Inamur Rahman[1,*]

[1]Research Lab-B043, Department of Chemistry, Integral University, 226026 Lucknow, Uttar Pradesh, India
[2]Research and Development in Construction Chemicals, CO2 and Waste Utilized Building Materials/Nanomaterials, CSIR-Central Building Research Institute, Ministry of Science and Technology, Govt. of India, 247667 Roorkee, Uttarakhand, India
[3]Department of Engineering, School of Computing, Engineering and Mathematical Sciences, La Trobe University, Melbourne, VIC 3086, Australia
[4]Department of Physical-AI, Jeonbuk National University, 54896 Jeonju, Republic of Korea
[5]Department of Physics, Integral University, 226026 Lucknow, Uttar Pradesh, India
[6]King Abdullah Institute for Nanotechnology, King Saud University, 11451 Riyadh, Saudi Arabia
*Correspondence: shaheerakhtar@jbnu.ac.kr (M Shaheer Akhtar); qirahman@iul.ac.in (Qazi Inamur Rahman)
Academic Editor: Carmen-Georgeta Ristoscu
Submitted: 30 April 2026 Revised: 29 June 2026 Accepted: 8 July 2026 Published: 11 November 2026

Abstract

Background: Textile industry effluents often contain nonbiodegradable dyes and other hazardous contaminants, causing severe pollution, eutrophication, and aesthetic quality deterioration of aquatic systems. Photocatalytic degradation is a promising wastewater treatment method involving the oxidative breakdown of dyes into less harmful smaller molecules under irradiation. **Methods:** Graphitic carbon nitride (g-C_3N_4) synthesized via the thermal polymerization of urea and ZnO nanorods (NRs) prepared through coprecipitation, followed by controlled thermal aging and calcination, were compared in terms of their performance for the degradation of model cationic (malachite green) and anionic (Congo red) dyes under natural sunlight irradiation. **Results:** g-C_3N_4 had a semicrystalline layered structure, optical bandgap of 2.68 eV, and zeta potential of −24.3 mV, while ZnO-NRs had a highly crystalline hexagonal wurtzite structure, optical bandgap of 3.09 eV, and zeta potential of −26.6 mV. The photodegradation efficiencies achieved by g-C_3N_4 after 150 min markedly exceeded those achieved by ZnO-NRs (malachite green: 90.21% vs. 66.78%, Congo red: 89.26% vs. 63.75%). Photodegradation exhibited pseudo-first-order kinetics, and the corresponding rate constants for g-C_3N_4 exceeded those for ZnO-NRs (malachite green: 0.01402 min^{-1} vs. 0.0071 min^{-1}, Congo red: 0.01209 min^{-1} vs. 0.00691 min^{-1}). The superior photocatalytic activity of g-C_3N_4 was primarily attributed to its narrower bandgap, improved visible-light absorption, layered conjugated structure, and efficient generation of reactive oxygen species under sunlight irradiation. **Conclusion:** g-C_3N_4 is a more effective visible-light-active photocatalyst than ZnO-NRs, holding promise for sustainable solar-driven wastewater treatment and environmental remediation.

Keywords: graphitic carbon nitride; zinc oxide; photocatalytic degradation; malachite green; Congo red; visible-light photocatalysis; sunlight irradiation

1. Introduction

The rapid and uncontrolled growth of the human population is linked to unplanned industrial expansion, which has led to unsound environmental problems worldwide. Among these issues, water contamination remains one of the most critical concerns. Although water is an indispensable resource for all living organisms, water scarcity and contamination affect more than 40% of the global population [1,2,3,4]. Industrial effluents comprise a wide range of hazardous pollutants, including organic dyes, heavy metals, pesticides, and various industrial chemicals, which significantly contribute to water contamination. Among these pollutants, malachite green (MG), a cationic triphenylmethane dye, and Congo red (CR), an anionic azo dye, are extensively used in textile, paper, leather, printing, and aquaculture industries owing to their complex aromatic structures, intense coloration, and chemical stability. However, the discharge of these dyes into aquatic environments poses serious environmental and health hazards because of their toxic, mutagenic, carcinogenic, and non-biodegradable nature.

Annually, the textile industry utilizes over 100,000 tons of organic dyes, of which nearly 15% are released into water bodies without sufficient treatment. The discharge of these dye-containing effluents causes environmental pollution, ecological imbalance, aesthetic deterioration of aquatic systems, and eutrophication, ultimately exerting harmful effects on aquatic flora and fauna [5,6,7,8,9,10]. Due to their high chemical stability, complex molecular structures, intense coloration, and poor biodegradability, organic dyes persist as contaminants in aquatic environments. Conventional wastewater treatment methods,

Copyright: © 2026 The Author(s). Published by IMR Press.
This is an open access article under the CC BY 4.0 license.

Publisher's Note: IMR Press stays neutral with regard to jurisdictional claims in published maps and institutional affiliations.

such as membrane filtration, sedimentation, coagulation, and flocculation, have been widely employed; however, these techniques often transfer contaminants from the liquid phase to the solid phase, generating sludge that requires further treatment and disposal [11,12]. On the contrary, the advanced oxidation processes, particularly heterogeneous photocatalysis, offer an efficient and sustainable solution to combat these issues [13,14,15]. Nonetheless, the indiscriminate discharge of untreated industrial effluents poses a serious threat to human health and aquatic ecosystems, emphasizing the need to develop photocatalytic decomposition and mineralization as an effective and sustainable solution for water purification [16,17]. In this context, the use of visible-light-driven photocatalysts under natural sunlight for water treatment offers a sustainable approach to pollution mitigation while supporting the achievement of the Sustainable Development Goals (SDGs), particularly those related to clean water and sanitation, affordable and clean energy, and responsible consumption and production (SDGs 6, 7, and 12) [18,19]. The performance of a photocatalytic system largely depends on the selection of an appropriate catalyst, which should be chemically stable, non-toxic, cost-effective, and capable of efficiently utilizing solar irradiation while effectively interacting with organic pollutants [20,21]. Among the various semiconductor photocatalysts studied, graphitic carbon nitride (g-C_3N_4) and ZnO have gained prominence as references owing to their complementary physicochemical and electronic properties [22,23]. A comparative evaluation of these materials offers valuable insights into the role of morphological, optical, and electronic characteristics in governing dye degradation under natural sunlight.

The g-C_3N_4 is a metal-free polymeric semiconductor with a layered structure composed of conjugated heptazine units. Its sp^2-hybridized π-conjugated framework and nitrogen lone-pair electrons facilitate visible-light absorption and result in a moderate band gap of approximately 2.7 eV. Among the various carbon nitride allotropes, g-C_3N_4 is particularly attractive due to its excellent thermal and chemical stability, natural abundance, and low toxicity, which collectively make it a promising candidate for solar-driven environmental remediation applications [24,25]. The structural concept of carbon nitride was first proposed by Liu and Cohen in 1989 [26] through the substitution of silicon in β-Si_3N_4, leading to the theoretical prediction of the β-C_3N_4 phase, which was suggested to exhibit a hardness potentially exceeding that of diamond. Although this phase remains hypothetical, it stimulated extensive research into carbon nitride materials. Since then, g-C_3N_4 has been widely synthesized using simple thermal polycondensation methods. For instance, Yu and Wang [27] synthesized g-C_3N_4 via direct microwave heating of melamine and artificial graphite at approximately 560 °C for 10 min and compared it with g-C_3N_4 prepared by conventional thermal polymerization of melamine at 550 °C for 4 h. The microwave-synthesized g-C_3N_4 exhibited excellent photocatalytic activity toward the degradation of rhodamine B and methyl orange under visible-light irradiation ($\lambda > 420$ nm). Subsequently, Ke et al. [28] synthesized a series of g-C_3N_4 materials through thermal condensation of melamine at 450–700 °C and observed that higher calcination temperature improved their photocatalytic activity under visible light (with a 1000 W xenon lamp) for degradation of rhodamine B and methyl orange, while maintaining good structural stability.

Further studies have demonstrated that the photocatalytic performance of g-C_3N_4 is highly dependent on the nature of precursor materials and synthesis conditions, such as precursor concentration, calcination temperature, and duration. These parameters critically influence the resulting morphology and crystallinity, thereby modulating and enhancing its photocatalytic activity [29,30,31]. In parallel, ZnO, due to its high exciton binding energy, excellent chemical stability, strong oxidation potential, and biocompatibility, functions as a robust metal-oxide photocatalyst for comparative evaluation. It also exhibits versatile morphological control, which can be systematically tuned through synthesis techniques such as sol-gel, coprecipitation, solvothermal, hydrothermal, and green methods [32,33].

Among these, rod-shaped ZnO nanostructures are particularly advantageous due to their robust crystallinity, increased surface area, directional charge transport, and minimized charge recombination, leading to improved photocatalytic performance. Prior studies reported that highly crystalline ZnO nanoparticles (20–30 nm) synthesized via the solution phase precipitation method exhibited ~95% degradation of rhodamine B under ultraviolet (UV) light, whereas the green-synthesized ZnO nanoparticles displayed improved degradation towards methylene blue/MG under natural sunlight [34,35]. Interestingly, ZnO morphology can be tuned by varying the pH, with alkaline conditions favoring the formation of rod-shaped nanostructures [36].

Despite significant progress on g-C_3N_4 and ZnO-based photocatalysts, most studies have focused on doped or composite systems, often employing artificial light sources and complex synthesis protocols to enhance performance. Consequently, systematic and comparative investigations of pristine g-C_3N_4 and ZnO nanostructures, synthesized via simple, template-free, and environmentally benign methods, along with evaluation of their photocatalytic behavior under natural sunlight exposure, remain relatively scarce.

Moreover, a comparative understanding of the role of band gap energy, morphology, surface charge characteristics, and dye-catalyst interaction towards the photocatalytic performance of both cationic and anionic dyes is still insufficiently explored.

Herein, we aim to develop simple, sustainable, and efficient photocatalytic systems for environmental remedi-

ation. Accordingly, visible-light active g-C_3N_4 is synthesized via thermal polymerization of urea, while rod-shaped ZnO-nanorods (NRs) are prepared using a coprecipitation method, with zinc acetate dihydrate (ZAD) as the precursor. A systematic comparative investigation of their structural, morphological, optical, and photocatalytic properties is conducted. The photocatalytic performance of both materials is evaluated for the degradation of cationic MG and anionic CR dyes under open-air natural sunlight exposure. The photocatalytic degradation behavior was further correlated with their band gap energies, surface charge characteristics, and kinetic parameters to understand the influence of physicochemical properties on photocatalytic performance. This comparative study provides valuable insights into the role of material composition, morphology, and surface charge in sunlight-driven photocatalysis, highlighting the potential of g-$C_3N_4$and ZnO-NRs for practical wastewater treatment applications.

2. Materials and Methodology

2.1 Chemicals

All chemicals used in this study were of analytical reagent grade and were used without further purification. ZAD [$Zn(CH_3COO)_2 \cdot 2H_2O$, CAS No. 5970-45-6, ≥99.5% purity] and urea [$CO(NH_2)_2$, CAS No.57-13-6, ≥99.5% purity] were procured from Sisco Research Laboratories Pvt.Ltd. (SRL, Mumbai, India) through Gyan Scientific, Lucknow, Uttar Pradesh, India. Sodium hydroxide (NaOH, CAS No.1310-73-2, ≥99.5% purity) and ethanol (C_2H_5OH, CAS No.64-17-5, ≥99.5% purity) were procured from Thermo Fisher Scientific India Pvt. Ltd., Mumbai, India, and MSB Chemical Ltd., Nagpur, India, respectively.

CR, an anionic azo dye [$C_{32}H_{22}N_6Na_2O_6S_2$, CAS No. 573-58-0], and MG, a cationic triphenylmethane dye [$C_{23}H_{25}ClN_2$, CAS No. 569-64-2], were used as model organic pollutants for the photocatalytic degradation studies and procured from HiMedia Laboratories Pvt. Ltd., Dindori, Nashik, India. Deionized (DI) water with a resistivity of 18.2 MΩ.cm at 25 °C, obtained from the Central Instrumentation Facility (CIF), Integral University, India, was used throughout the experimental work.

2.2 Synthesis of g-C_3N_4 and ZnO-NRs

The g-C_3N_4 was synthesized via the thermal condensation of urea. In a typical procedure, 15 g of urea was placed in an aluminum foil-covered alumina crucible and heated in a muffle furnace at 580 °C for 150 min at a heating rate of 5 °C min^{-1} under ambient air atmosphere. The temperature of 580 °C was selected based on literature reports [28,29] for the efficient synthesis of crystalline g-C_3N_4 with improved photocatalytic activity. During thermal treatment, urea underwent polymerization and condensation, yielding a pale-yellow solid, which indicates the formation of g-C_3N_4. After naturally cooling to room temperature, the obtained product was thoroughly washed with ethanol to remove unreacted residues and surface impurities. The material was subsequently dried in an oven at 100 °C for 1 h to obtain a stable powder, following reported procedures. The final product was designated as g-C_3N_4. A schematic illustration of the synthesis process is shown in Fig. 1a.

ZnO-NRs were synthesized using the coprecipitation method, as schematically illustrated in Fig. 1b Initially, a 0.2 M ZAD solution was prepared by dissolving 8.77 g of the precursor in 200 mL of DI water (initial pH = 6.14 at 37.9 °C). Subsequently, 100 mL of 0.4 M NaOH solution was added dropwise under continuous stirring until the pH reached 10.41 at 43.4 °C. The experimental Zn:NaOH molar ratio was maintained at 1:1. The pH of the reaction mixture was continuously monitored using a digital pH meter during the addition of NaOH. To prevent particle aggregation, 100 mL of absolute ethanol was introduced into the reaction mixture under continuous stirring. Ethanol acted as a capping agent, facilitating homogeneous mixing and minimizing nanoparticle agglomeration. The resulting suspension was transferred to a three-neck flask and heated at 80 °C for 4 h under continuous stirring to facilitate controlled crystal growth and obtain a uniform ZnO morphology. The chemical reactions involved are presented in Eqns. 1,2,3.

$$Zn(CH_3COO)_2 \cdot 2H_2O + 2NaOH \rightarrow Zn(OH)_2 \downarrow + 2CH_3COONa + 2H_2O \quad (1)$$

$$Zn(OH)_2 + 2OH^- \rightarrow Zn(OH)_4^{2-} \quad (2)$$

$$Zn(OH)_4^{2-} \rightarrow ZnO + H_2O + 2OH^- \quad (3)$$

After completion of the reaction, the mixture was allowed to cool overnight, followed by filtration and successive washing with DI water and then with ethanol. The obtained precipitate was dried in an oven at 80 °C for 1 h to remove residual solvent and moisture, and subsequently calcined in a muffle furnace at 400 °C for 2 h under ambient air atmosphere using a heating rate of 5 °C min^{-1}. The morphology of the synthesized ZnO-NRs was influenced by synthesis parameters such as solution pH, NaOH addition rate, calcination temperature, and duration, as well as the presence of ethanol, which acts as a capping agent and enhances stability and purity. The final product was denoted as ZnO-NRs.

2.3 Material Characterizations

The crystal structure and phase purity of the synthesized materials were analyzed using an X-ray diffractome-



Fig. 1. Schematic illustration of the synthesis of (a) g-C_3N_4 by thermal condensation of urea and (b) ZnO-NRs by coprecipitation of zinc acetate dihydrate with NaOH, and subsequent calcination.

ter (MiniFlex 600C, Benchtop Rigaku, Akishima, Tokyo, Japan) equipped with Cu Kα radiation (λ = 1.5418 Å), operated at 40 kV and 15 mA. Diffraction patterns were recorded over a 2θ range of 10–80 °, at a scan rate of 4° min^{-1} with step size of 0.01°. The obtained diffraction data were analyzed using Rigaku-PDXL software (version 2.x). Functional groups were identified by Fourier-transform infrared spectroscopy (FTIR, Spectrum IR, PerkinElmer, Waltham, MA, USA) using the KBr pellet method. The spectra were recorded at a resolution of 4 cm^{-1} with 32 accumulated scans and were processed through the Spectrum Version 10.1.00 software. Surface morphology and elemental composition were examined using field-emission scanning electron microscopy (FESEM) (JEOL JSM-7100F, JEOL Ltd, Tokyo, Japan) coupled with energy-dispersive X-ray spectroscopy (EDS). The morphology of g-C_3N_4 was analyzed using a Nova NanoSEM 450 (FEI Company, Hillsboro, OR, USA) at an accelerating voltage of 15.0 kV and a working distance of approximately 4.7 mm, whereas ZnO-NRs were analyzed using a FE-SEM at an accelerating voltage of 10.0 kV and a working distance of approximately 15.9 mm. Hydrodynamic particle size and zeta potential were measured using a Malvern Zetasizer (ZSU3305, Malvern Instruments Ltd., Malvern, Worcestershire, UK). Samples were dispersed in DI water, probe-sonicated for 1 min to obtain a homogenous suspension, and analyzed at 25 °C. Measurements were performed in triplicate, and average values were reported. The obtained hydrodynamic particle size and zeta potential data were analyzed using Zetasizer software. The optical behavior was analyzed using Ultraviolet (UV)-visible diffuse reflectance spectroscopy (UV-DRS, Lambda 750 Perkin-Elmer, USA) in the wavelength range of 200–800 nm, using $BaSO_4$ as the reference standard. UV-visible absorption spectra were recorded using a Shimadzu UV-1700 spectrophotometer, in the range of 200–800 nm with DI water as the reference. The degradation intermediates and products formed during photocatalytic dye decomposition were identified using liquid chromatography-mass spectrometry (LC-MS, 6475 Triple Quadrupole LC-MS, Agilent Technologies, USA). Photoluminescence (PL) spectra were recorded using a JASCO fluorescence spectrophotometer (FP-6500, Japan) at ambient temperature with an excitation wavelength of 350 nm and emission range of 380–800 nm with scanning resolution of 0.5 nm.

2.4 Photocatalytic Activity

The photocatalytic activities of the synthesized g-C_3N_4 and ZnO-NRs were evaluated against CR and MG dyes under open-air sunlight exposure. A 10 ppm solution of each dye was prepared in 500 mL of DI water. For each experiment, 100 mg of the photocatalyst was dispersed in 100 mL of the dye solution contained in an uncovered 200 mL glass beaker. The initial pH values of MG and CR dye solutions were 6.86 and 6.61, respectively. After the addition of photocatalysts, slight variations in pH

were observed. Before sunlight irradiation, the suspension was stirred in the dark at approximately 200 rpm for 20 min to establish adsorption-desorption equilibrium. To ensure uniform light exposure and homogeneous suspension of photocatalyst particles, the reaction mixture was continuously stirred throughout the experiment at approximately 200 rpm, and the position of the reaction vessel was periodically adjusted during sunlight exposure.

The photocatalytic degradation experiments were conducted at the Department of Chemistry, Integral University, Lucknow, India, during 14–16 May under clear weather conditions between 10:30 AM and 2:00 PM (IST). The experiments were carried out under natural sunlight. Solar irradiance was not directly measured during the experiments. It has been reported in literature that the irradiance ranging 650–800 Wm^{-2} was recorded in clear-sky solar radiation data under similar climatic conditions [37,38]. During the experiments, the reaction temperature was maintained in the range of 37–40 °C. A limitation of the present study is that real-time solar irradiance was not monitored; therefore, minor variations in sunlight intensity during the experiment period cannot be excluded.

The photocatalytic studies were repeated twice under similar experimental conditions, and the average values were reported. The progress of the photocatalytic degradation reaction was monitored using a UV-visible spectrophotometer (Shimadzu UV-1700) by recording the absorbance of the degraded dye solution at regular intervals of 25 min. Before UV-visible analysis, the suspended photocatalyst particles were separated by centrifugation at 4500 rpm for 5 min. Control experiments were also performed under similar conditions without a photocatalyst to evaluate non-photocatalytic effects. The efficiency of dye degradation was analyzed based on the changes in absorbance intensity over time.

3. Results

3.1 Structural and Functional Group Analysis

The crystalline structures of g-C_3N_4 and ZnO-NPs were characterized by X-ray diffraction (XRD), as shown in Fig. 2a The XRD pattern of g-C_3N_4 exhibits two characteristic diffraction peaks: a weak peak at ~13.1° and an intense peak at ~27.4°, corresponding to the (100) plane and (002) crystallographic planes, respectively, as shown in Fig. 2a(i). The weak diffraction peak is attributed to the in-plane structural packing of tri-s-triazine units, whereas the intense peak arises from interlayer π-π stacking of the conjugated aromatic layer in g-C_3N_4 sheets [22]. The relatively broad nature of these reflections indicates the semicrystalline and layered structure of thermally polymerized carbon nitride. The crystallite size of g-C_3N_4, enumerated using the Scherrer equation from the (002) diffraction peak, was found to be approximately 10 nm.

In contrast, the XRD pattern for ZnO-NRs is shown in Fig. 2a(ii) exhibits sharp and intense diffraction peaks at 31.7°, 34.4°, 36.2°, 47.5°, 56.6°, 62.8°, 66.3°, 67.9°, 69.1°, 72.5°, and 76.8°, which are indexed to the (100), (002), (101), (102), (110), (103), (200), (112), (201), (004), and (202) planes, respectively corresponding to the hexagonal wurtzite structure of ZnO (JCPDS 36-1451) [34]. The absence of additional impurity peaks further confirms the phase purity of the synthesized ZnO-NRs.

The average crystallite size calculated using the Scherrer equation was found to be 20.94 ± 0.69 nm, while the average inter-planar spacing (d-spacing) was estimated to be 1.801 ± 0.154 Å. Furthermore, various crystallographic parameters, including crystallite size, d-spacing, dislocation density (δ), and microstrains (ε), were enumerated by analyzing the XRD data and presented in Table 1.

The relatively low values of microstrain ($3.75 \pm 0.33 \times 10^{-3}$) and dislocation density ($2.35 \pm 0.15 \times 10^{-3}$ nm^{-2}) indicate reduced lattice distortion and fewer crystallographic defects, thereby confirming the good crystallinity and structural stability of the synthesized ZnO-NRs. The XRD analysis confirms the successful synthesis of semicrystalline g-C_3N_4 and highly crystalline ZnO-NRs, exhibiting their respective structural characteristics.

The FTIR spectra of g-C_3N_4 and ZnO-NRs are shown in Fig. 2b exhibit distinct vibrational features corresponding to their respective structural frameworks. For clarity, the major FTIR peaks and their corresponding functional groups are summarized in Table 2 (Ref. [22,24,32,33,39]). The FTIR spectrum of g-C_3N_4 shows a broad absorption band in the region of 3282–3095 cm^{-1}, attributed to the stretching vibrations of terminal N-H groups along with minor contributions from surface-adsorbed O-H groups. A comparatively sharper band observed at ~3164 cm^{-1} corresponds to N-H stretching vibrations associated with residual amine functionalities in the heptazine framework [22,24]. Similar vibrational features have been widely reported for g-C_3N_4 synthesized through thermal polymerization of nitrogen-rich precursors [39]. Additionally, the multiple absorption bands appearing in the region 1646–1218 cm^{-1} are assigned to the characteristic stretching vibrations of C=N and C-N heterocycles within tri-s-triazine/heptazine units, representing the fingerprint region of polymeric g-C_3N_4. However, the absorption band appearing in the region of 897–815 cm^{-1} corresponds to the breathing vibration mode of the tri-s-triazine ring, confirming the successful formation of g-C_3N_4 framework [22,24].

On the contrary, ZnO-NRs spectrum is dominated by metal-oxygen and surface-related vibrational modes. The broad absorption centered at ~3246 cm^{-1} is attributed to O-H stretching vibration arising from surface hydroxyl groups and physically adsorbed moisture, which are commonly observed in oxide nanostructures. The bands appearing in the region of 1566–1547 cm^{-1} are associated with $C{=}O/COO^-$ stretching vibrations, indicating the presence of residual organic species or surface-bound ethanol-derived residues during synthesis. Notably, the strong absorption band ob-

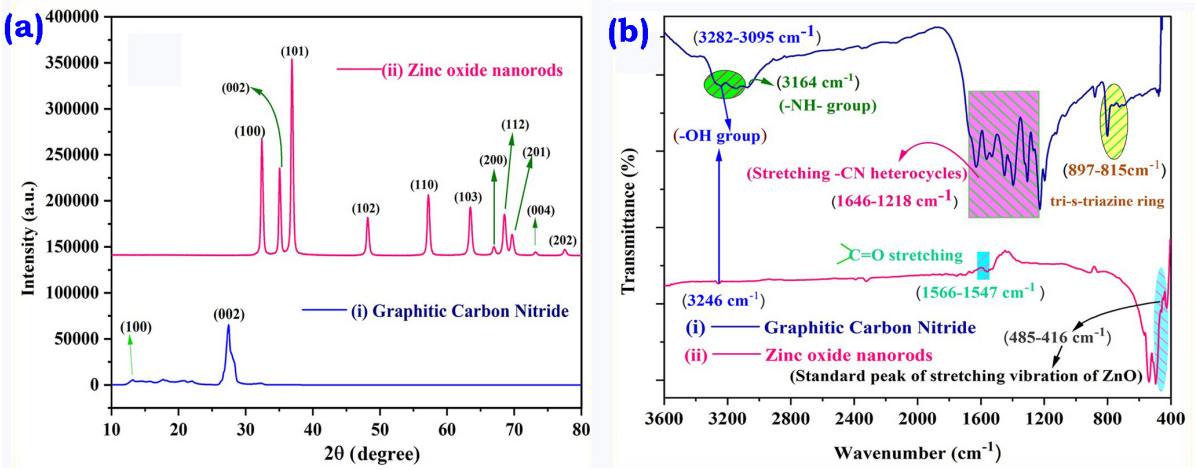


Fig. 2. Structural and functional group analysis of g-C_3N_4 and ZnO-NRs. (a) XRD patterns of g-C_3N_4 and ZnO-NRs showing characteristic diffraction peaks of polymeric g-C_3N_4 and hexagonal wurtzite ZnO. (b) Fourier-transform infrared spectroscopy (FTIR) spectra of g-C_3N_4 and ZnO-NRs confirming the formation of polymeric g-C_3N_4 and crystalline ZnO. XRD, X-ray diffraction.

Table 1. Various crystallographic parameters derived from XRD analysis of synthesized ZnO-NRs.

Peak (hkl)	2θ°	FWHM (β)	Crystallite size (nm) $D = \frac{0.9\lambda}{\beta \cos\theta}$	Dislocation density $\delta = \frac{1}{D^2} \times 10^{-3}(nm^{-2})$	Microstrain $\varepsilon = \frac{\beta}{4 \tan\theta} \times (10^{-3})$	d-spacing (Å)
(100)	31.7	0.378	22.65	1.95	5.6	2.821
(002)	34.4	0.364	23.76	1.77	4.93	2.605
(101)	36.2	0.39	22.17	2.03	5.03	2.48
(102)	47.5	0.43	20.75	2.32	4.15	1.912
(110)	56.6	0.446	20.76	2.32	3.52	1.625
(103)	62.8	0.493	19.28	2.69	3.45	1.479
(200)	66.3	0.533	18.12	3.04	3.5	1.409
(112)	67.9	0.524	18.62	2.88	3.33	1.38
(201)	69.1	0.547	17.97	3.1	3.37	1.358
(004)	72.5	0.4	24.74	1.63	2.15	1.304
(202)	76.8	0.473	21.54	2.15	2.2	1.24

FWHM, full width at half maximum.

Table 2. FTIR spectral assignments of synthesized g-C_3N_4 and ZnO-NRs with associated functional groups.

Material	Wavenumber (cm^{-1})	Peak assignment	Functional group/vibration	Reference
g-C_3N_4	3282–3095	Broad stretching vibration	N-H/O-H stretching vibrations	[22,24]
	~3164	Stretching vibration	Residual amine (-NH/-NH_2) groups	[22,24]
	1646–1218	Multiple stretching bands	C=N and C-N stretching of heterocyclic heptazine units	[22,24]
	897–815	Ring breathing vibration	Tri-s-triazine/heptazine ring	[39]
ZnO-NRs	~3246	Broad stretching vibration	Surface O-H stretching vibrations from adsorbed water/hydroxyl groups	[32,33]
	1566–1547	Stretching vibration	C=O/COO^- vibrations from residual organic species.	[32,33]
	485–416	Metal–oxygen vibration	Zn–O Stretching vibration	[32,33]

FTIR, Fourier-transform infrared spectroscopy.

served in the region of 485–416 cm^{-1} corresponds to the characteristic Zn-O stretching vibration, confirming the formation of crystalline ZnO-NRs [32,33]. Only slight peak shifts from reported values were observed, owing to synthesis conditions, crystallinity, hydroxylation, and nanoscale structural variations.

The FTIR spectra clearly substantiate the synthesis of polymeric g-C_3N_4 and ZnO-NRs, exhibiting their characteristic structural functionalities.

3.2 Morphological and Compositional Analysis

The comparative SEM analysis of g-C_3N_4 is shown in Fig. 3a,b and ZnO-NRs depicted in Fig. 3e,f highlights the distinctly different morphological architectures of the synthesized materials. The g-C_3N_4 exhibits a highly aggregated, sheet-like morphology composed of irregularly stacked and wrinkled sheets that assemble into loose, porous agglomerates. The sheets possess a rough and granular surface texture with evident turbostratic disorder, which is consistent with the semicrystalline nature inferred from XRD analysis. In contrast, ZnO-NRs exhibit a well-defined rod-to-needle-like morphology, with uniformly grown nanorods displaying hexagonal facets characteristic of the wurtzite ZnO crystal structure. Their smooth facets, sharp edges, and geometric regularity indicate high crystallinity, which is consistent with the sharp and intense diffraction peaks observed in the XRD pattern. The formation of uniform ZnO-NRs further suggests controlled nucleation and anisotropic crystal growth during thermal aging, facilitated by the capping agent.

The distinct morphological differences between g-C_3N_4 and ZnO-NRs were expected to significantly influence their photocatalytic behavior. The porous layered structure of g-C_3N_4 offers a relatively high-surface-area and abundant active sites, whereas ZnO-NRs contribute crystalline, high-aspect-ratio nanorods that can facilitate directional charge transport along their polar facets and improved separation of photogenerated charge carriers.

The particle size distribution histogram displayed in Fig. 3c and Fig. 3g; the size histogram of g-C_3N_4 shows an average particle size of ~144.02 nm with a standard deviation of 27.16, with moderate dispersion, while ZnO-NRs in Fig. 3g exhibit an average rod length of ~584 nm, confirming the successful anisotropic growth of ZnO-NRs. The corresponding energy-dispersive X-ray spectroscopy (EDX) spectra and quantitative analyses revealed in Fig. 3d,h show that g-C_3N_4 consists primarily of C (72.58 wt%, 75.54 at%) and N (27.42 wt%, 24.46 at%) without detectable impurity peaks, confirming the successful formation of polymeric g-C_3N_4. In contrast, the ZnO-NRs show dominant Zn (78.1 wt%, 46.7 at%) and O (21.9 wt%, 53.4 at%) signals, verifying the formation of phase-pure ZnO-NRs with near stoichiometric composition.

These results conclusively confirm the presence of semicrystalline layered g-C_3N_4 sheets and highly crystalline ZnO-NRs, both exhibiting distinct morphological and compositional characteristics suitable for photocatalytic applications.

3.3 Optical and Optoelectronic Properties

The optical band gap energies of g-C_3N_4 and ZnO-NRs were estimated using the Tauc equation in combination with the Kubelka-Munk function, where the absorption coefficient (α) for powdered samples was replaced by the Kubelka-Munk function, $F(R) = (1 – R)^2 / 2R$. The band gap energy (E_g) was determined by extrapolating the linear region of the Tauc plots to the energy axis [40].

For g-C_3N_4, the Tauc plot analysis is shown in Fig. 4a was demonstrated using the expression $(F(R)\cdot h\nu)^{1/2}$, corresponding to an indirect allowed electronic transition. The extrapolation of the linear region yields a band gap energy of approximately 2.68 eV. This value is consistent with previously reported band gap values for thermally polymerized g-C_3N_4 (2.6–2.9 eV), corroborating its ability to tune with visible-light driven photocatalytic applications. The slight decrease in band gap energy may be attributed to structural defects and enhanced electronic conjugation within the heptazine framework.

For ZnO-NRs, the Tauc plot shown in Fig. 4b was analyzed using the expression $(F(R)\cdot h\nu)^2$, attributed to a direct allowed transition, since ZnO is a well-known direct band gap semiconductor. The extrapolation of the linear region gives an optical band gap of approximately 3.09 eV. This value is slightly lower than that of bulk ZnO (~3.37 eV), which may be associated with the presence of structural defects, oxygen vacancies, and surface-related states generated during the synthesis. Furthermore, the absorption tail observed in the lower energy region (2.8–3.1 eV) supports the existence of defect-induced localized states within the band structure.

To further examine the charge-carrier recombination behavior, PL spectra of both g-C_3N_4 and ZnO-NRs were recorded and presented in **Supplementary Fig. 1**. The obtained spectra exhibited characteristic emission bands for both photocatalysts. A comparatively higher PL intensity was observed for g-C_3N_4, which may be related to its intrinsic electronic structure and conjugated heptazine framework. The broad emission originates from structural defects on the catalyst surfaces, which might facilitate the generation of active sites for photocatalytic degradation. However, the PL results alone are insufficient to conclusively establish either superior charge-separation efficiency or suppressed electron-hole recombination. Therefore, the enhanced photocatalytic performance of g-C_3N_4 is primarily attributed to its narrower band gap, improved visible light absorption, and layered structural characteristics.

3.4 Surface Charge and Hydrodynamic Size Analysis

Photocatalysis reactions primarily occur at the surface of nanomaterials; therefore, the photocatalytic efficiency is strongly influenced by surface charge characteristics, adsorption behavior, dispersion stability, and the pH of the solution. From this perspective, zeta potential analysis provides an effective approach to evaluating surface charge behavior and colloidal stability of photocatalysts. The hydrodynamic particle size distribution and zeta potential of g-C_3N_4 and ZnO-NRs were measured at room temperature using DI water as the dispersant medium (dielectric constant: 78.5).

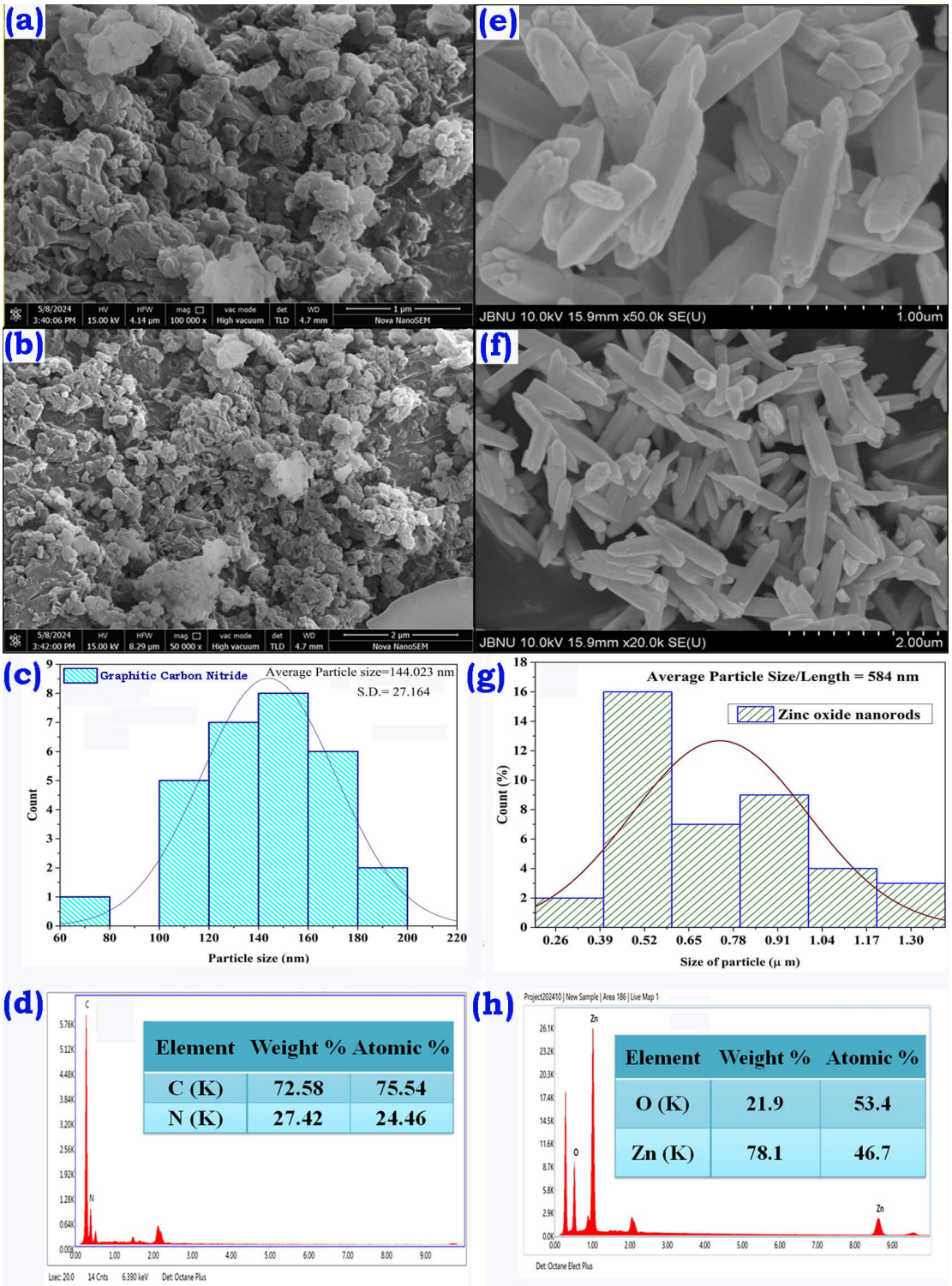


Fig. 3. Surface morphological features: FESEM images of (a,b) g-C_3N_4 showing wrinkled and aggregated sheet like morphology and (e,f) ZnO-NRs exhibiting uniform rod-like morphology, with corresponding (c,g) size distributions and (d,h) EDX spectra confirming elemental composition. FESEM, field-emission scanning electron microscopy; EDX, energy-dispersive X-ray. Scale bar = 1 μm in (a,e); scale bar = 2 μm in (b,f).

The dynamic light scattering (DLS) size distribution profiles presented in Fig. 5a and Fig. 5b revealed average hydrodynamic particle sizes of 496.7 nm for g-C_3N_4 and 1297.0 nm for ZnO-NRs, respectively. These hydrodynamic sizes are significantly larger than the particle sizes observed from FESEM and XRD analysis because DLS measures the effective hydrodynamic diameter of particles dispersed in aqueous medium, including the solvent/hydra-

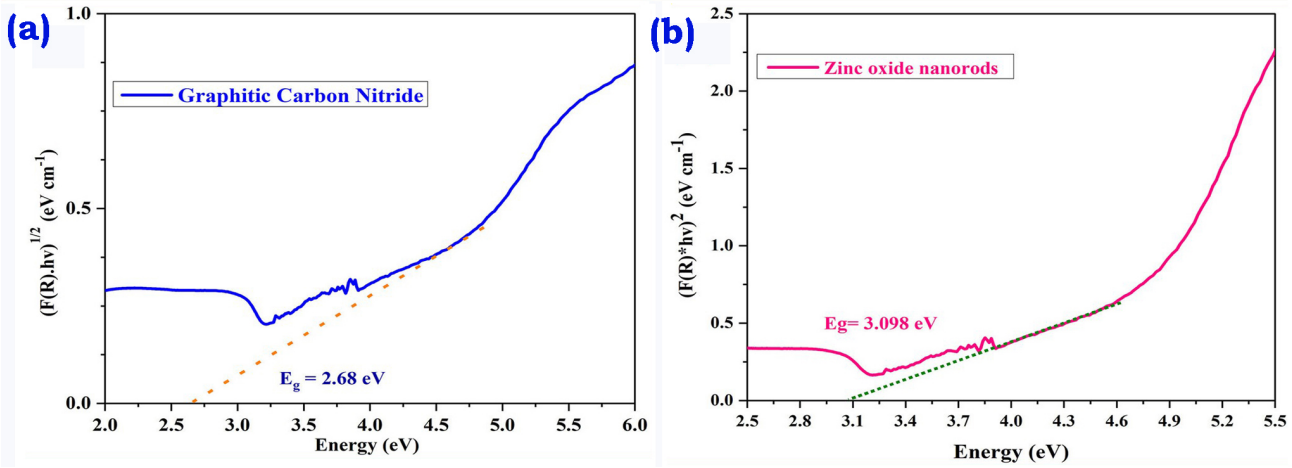


Fig. 4. Tauc plots of (a) g-C_3N_4 and (b) ZnO-NRs, showing optical band gap energies of ~2.68 eV and ~3.09 eV, respectively.

tion layer, electrical double layer, and agglomerated particle clusters, whereas, the FESEM and XRD provide the actual particle size under dry conditions. The larger DLS sizes further suggest partial aggregation of both photocatalysts in suspension owing to their high surface energy and interparticle interaction. The polydispersity index (PDI) values were found to be 0.244 for g-C_3N_4 and 0.584 for ZnO-NRs. The lower PDI value of g-C_3N_4 indicates relatively better dispersion with moderate particle-size distribution, whereas the higher value for ZnO-NRs suggests broader particle-size distribution and comparatively higher agglomeration behavior in the colloidal system. The corresponding zeta potential results depicted in Fig. 5c and Fig. 5d exhibited negative surface charge values of –24.3 mV for g-C_3N_4 and –26.6 mV for ZnO-NRs, respectively.

The negative zeta potential values attribute moderate electrostatic stabilization and colloidal stability of both photocatalysts in aqueous medium, which helps prevent excessive particle agglomeration during photocatalytic degradation studies.

3.5 Evaluation of Photocatalytic Potential of g-C_3N_4 and ZnO-NRs

Photocatalytic degradation performances of the synthesized g-C_3N_4 and ZnO-NRs were evaluated against MG and CR dyes under direct sunlight exposure, and the results are depicted in Fig. 6a–d. Fig. 6a,c illustrates the time-dependent UV-visible absorption spectra for MG dye degradation, whereas Fig. 6b,d corresponds to CR dye degradation using g-C_3N_4 and ZnO-NRs photocatalyst, respectively. It was observed that neither MG nor CR dye solutions exhibited noticeable degradation in the absence of photocatalysts under sunlight exposure, indicating negligible photolysis under the experimental conditions. However, upon addition of g-C_3N_4 and ZnO-NRs, a gradual decrease in the characteristic absorption intensity of MG (619 nm) and CR (498 nm) was observed with increasing the irradiation time, affirming the photocatalytic degradation capability of both synthesized materials. The photocatalytic degradation efficiency (DE) was enumerated using the following empirical equation [41,42,43];

$$DE(\%) = \left(1 - \frac{c_t}{c_0}\right) \times 100 \quad (4)$$

where C_0 and C_t represent the dye concentration (or corresponding absorbance value) at instant time t = 0 min and at a given irradiation time t, respectively. Fig. 6e shows the DE of MG dye, where g-C_3N_4 exhibited superior photocatalytic activity with 90.21% degradation within 150 min, whereas ZnO-NRs achieved 66.78% degradation under identical experimental conditions. Similarly, for CR dye DEs of 89.26% and 63.75% were obtained using g-C_3N_4 and ZnO-NRs, respectively, after 150 min of sunlight exposure, as shown in Fig. 6f. The DE of g-C_3N_4 was approximately ~1.35 and 1.40 times higher than that of ZnO-NRs for MG and CR dyes, respectively. The enhanced photocatalytic performance of g-C_3N_4 may be attributed to its narrower band gap energy (2.68 eV), improved visible-light absorption capability, and layered conjugated structure. Furthermore, electrostatic interactions between the negatively charged g-C_3N_4 surface and cationic MG molecules, together with possible π–π interactions between the dye molecules and the conjugated heptazine framework, may facilitate enhanced adsorption and improved DE.

Although both photocatalysts possess negative zeta potential values, appreciable degradation of anionic CR dye was also observed. This behavior suggests that electrostatic interactions were not the sole governing factor in the photocatalytic process. The degradation process relies on reactive oxygen species ($^{\bullet}OH$ and $^{\bullet}O_2^-$) generated on the catalyst surface under sunlight irradiation, which can effectively oxidize dye molecules even in the presence of electrostatic repulsion. Additionally, π-π interactions between

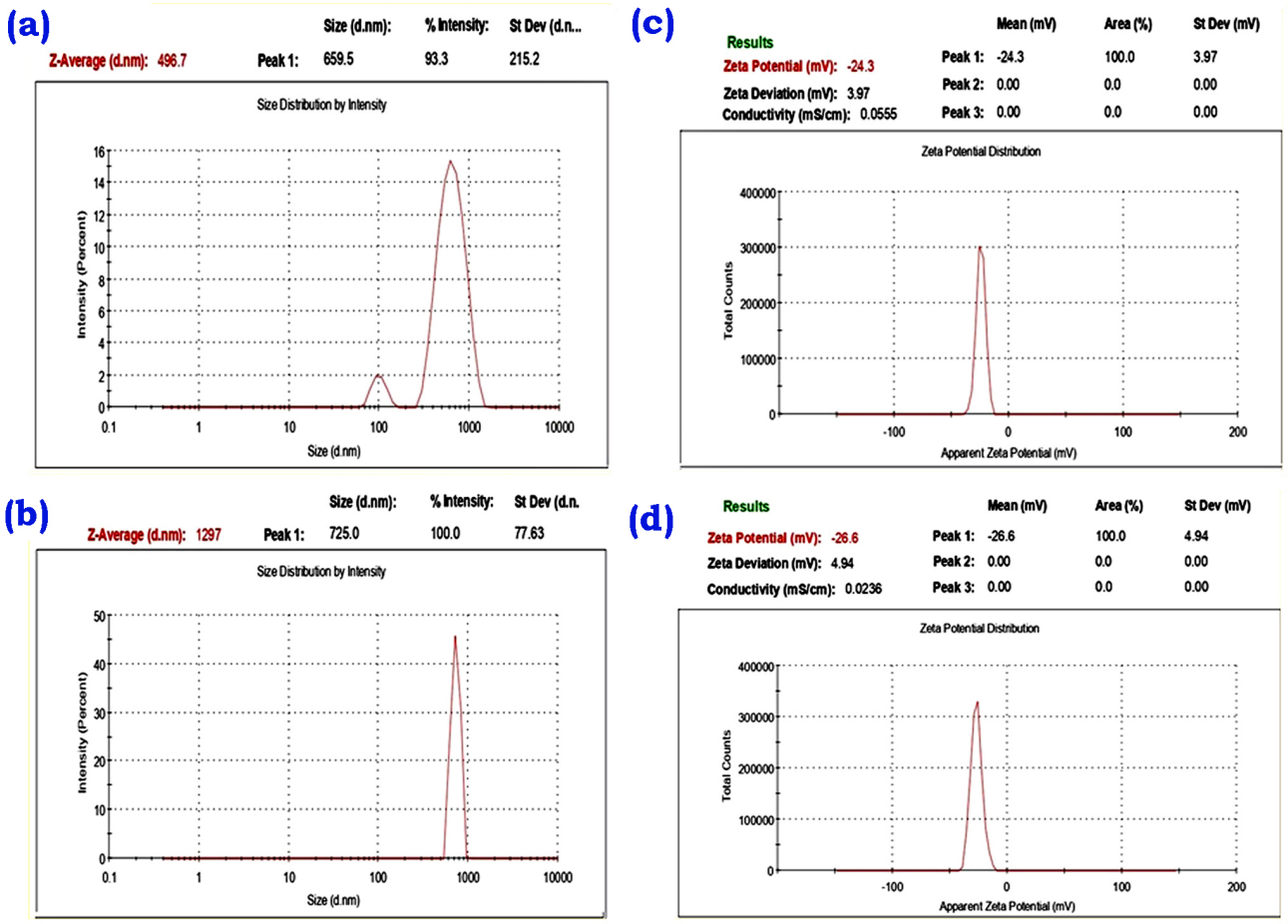


Fig. 5. DLS size distributions of (a) g-C_3N_4 and (b) ZnO-NRs and corresponding zeta potentials distributions (c) –24.3 mV and (d) –26.6 mV, indicating negatively charged, stable dispersions.

the aromatic structure of CR molecules and the conjugated g-C_3N_4 framework may further facilitate adsorption and degradation.

The kinetics of the photocatalytic degradation process were further analyzed using the pseudo-first-order model in accordance with empirical Eqn. 5.

$$ln\left(\frac{C_0}{C_t}\right) = kt \tag{5}$$

Fig. 6g,h illustrates the plots of ln (C_o/C_t) vs irradiation time, showing a good linear relationship for both dyes. The obtained linearity confirms that the degradation process follows pseudo-first-order reaction kinetics [44,45].

The apparent pseudo-first order rate constants (k) for MG degradation were determined to be 0.01402 min^{-1} for g-C_3N_4 and 0.0071 min^{-1} for ZnO-NRs. Similarly, for CR degradation, the corresponding rate constants were 0.01209 min^{-1} and 0.00691 min^{-1}, respectively. The higher rate constant values obtained for g-C_3N_4 further confirm its superior photocatalytic activity as compared to ZnO-NRs. A comparative analysis of DE, half-life ($t_{1/2}$), rate constant (k), and regression coefficient (R^2) values is summarized in Table 3. The relatively higher R^2 values indicate good agreement of experimental data with the pseudo-first-order reaction kinetic model.

Furthermore, the photocatalytic performances of the synthesized photocatalysts were compared with previously reported g-C_3N_4 and ZnO-based photocatalysts, as summarized in Table 4 (Ref. [46,47,48,49,50,51,52,53,54,55,56,57]). The synthesized g-C_3N_4 and ZnO-NRs exhibited comparable or enhanced photocatalytic activity under sunlight irradiation relative to previously reported works.

Moreover, the degradation process was further supported by LC-MS analysis of the degraded dye solution, which revealed the formation of multiple intermediate degradation products, as shown in **Supplementary Figs. 2,3**, indicating the progressive photocatalytic decomposition of dye molecules into lower molecular-weight and comparatively less harmful compounds, along with inorganic ions/mineral species.

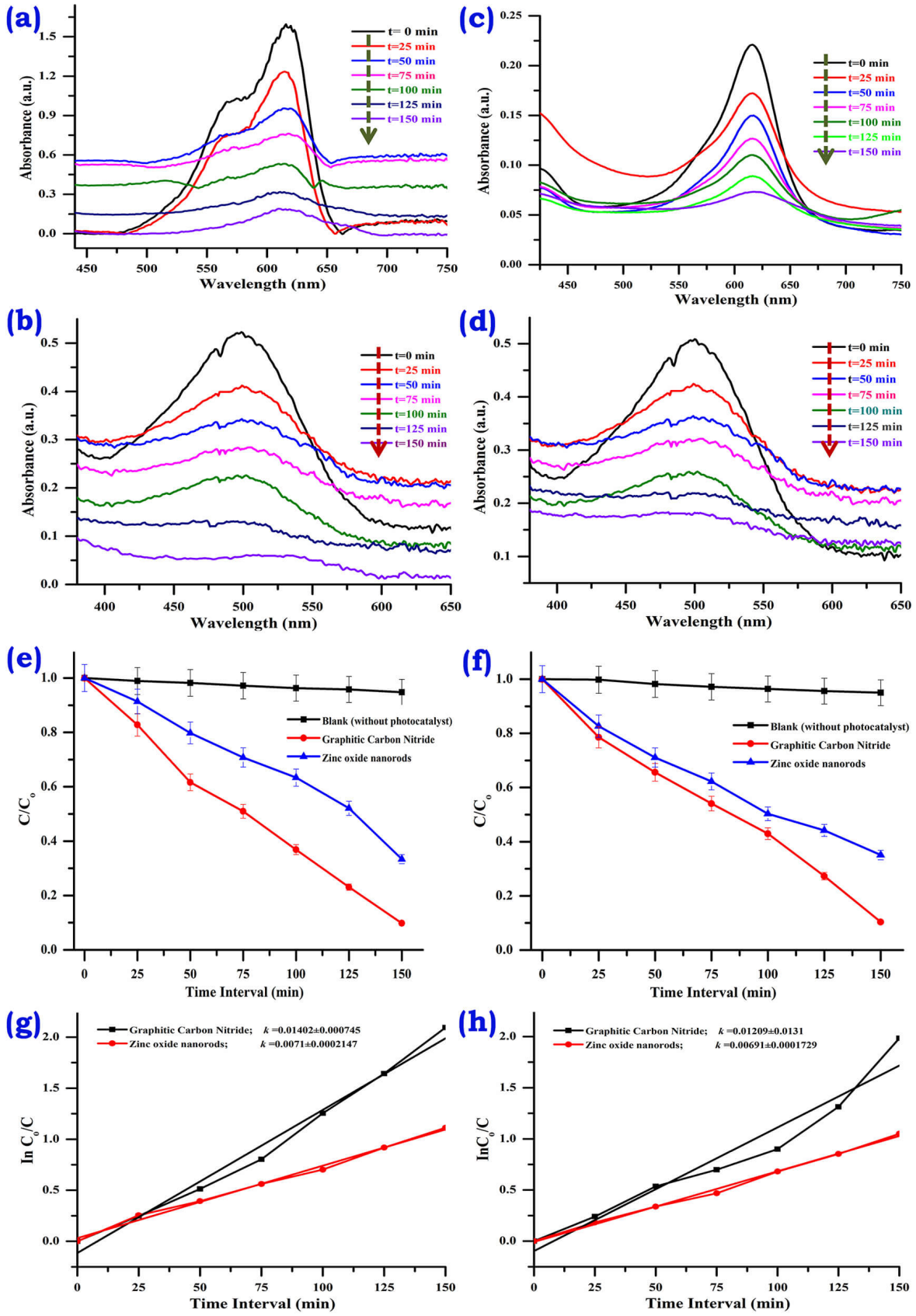


Fig. 6. Photocatalytic degradation of MG and CR under sunlight using g-C_3N_4 and ZnO-NRs: (a–d) time-dependent UV-visible spectra, (e,f) DEs, and (g,h) pseudo-first-order kinetic plots. CR, Congo red; MG, malachite green; UV-visible, ultraviolet-visible.

Table 3. Kinetic parameters for the photocatalytic degradation of MG and CR dyes using g-C_3N_4 and ZnO-NRs.

Photocatalyst (dose 0.1 g/100 mL)	Dyes	Degradation efficiency (%)	Half-life ($t_{1/2}$) (min)	Rate constant (min^{-1})	Regression coefficient (R^2)
g-C_3N_4	MG	90.21	49.45	0.01402	0.9094
	CR	89.26	57.34	0.01209	0.8582
ZnO-NRs	MG	66.78	97.60	0.00710	0.8995
	CR	63.75	100.32	0.00691	0.9947

Table 4. Comparison of photocatalytic efficiencies of g-C_3N_4 and ZnO-NRs with reported g-C_3N_4 and ZnO-based photocatalysts.

Photocatalyst	Raw material	Synthesis technique and reaction parameter	Pollutants, Concentration (mg/L)	Catalyst dose (g/L)	Source of light	DE (%), irradiation time (min)	k (min^{-1})	Ref.
g-C_3N_4	urea	Thermal polymerization	CR, 10 MG, 10	1 1	Open air Sunlight	89.26 90.21	0.01209 0.01402	This work
ZnO-NRs	ZAD	Coprecipitation 400 °C, 2 h	CR, 10 MG, 10	1 1		63.75 66.78	0.00691 0.00710	
g-C_3N_4-550 °C	urea	Calcination, 2 h	MB, 10	0.1	200 W Xe lamp	62.6, 120	0.0081	[46]
g-C_3N_4-550 °C	urea	Calcination, 550 °C, 3 h	MO CR XO PR RhB CV	0.1	200 W, Tungsten lamp	10, 120 13, 120 15, 120 26, 120 35, 120 51, 120	0.0008, 0.0012, 0.0013, 0.0024, 0.0029, 0.0062	[47]
g-C_3N_4	MEL	Calcination, 500 °C, 4 h	MV, 20	20 mg	300 W Xe lamp	55.80, 210	0.0033	[48]
2-D g-C_3N_4	MEL	Calcination	MB, 20	0.2	300 W, Xe lamp	21, 30	0.00743	[49]
g-C_3N_4	MEL	Pyrolysis	RhB, 23.95	1.0	Sunlight	95, 320	0.00936	[50]
5% S/g-C_3N_4	DCDA	Calcination, 550 °C, 3 h	MB, 20	0.1	300 W Xe lamp	60, 300	0.00135	[51]
S-g-C_3N_4	TU	Pyrolysis, 450 °C, 2 h	RhB, 10	0.5	1000 W, Xe lamp	37.86, 90	0.00508	[52]
c-ZnO-NPs	ZNH	Green route	MB, 20	0.24	UV lamp	56.5, 60	0.01015	[53]
ZnO	ZNH	Sol-gel method	CR, 50	1.0	Sunlight	94, 60	0.0222	[54]
ZnO	ZNH	Green route	RB, 30	0.24	30 W Hg lamp	85, 60	0.03162	[55]
ZnO	ZNH	One-pot green route	RhB, 10	0.5	500 W, Xe lamp	75, 120	NA	[56]
ZnO-NPs	ZAD	Coprecipitation method	RB, 40	0.5	300 W, Xe lamp	49, 120	NA	[57]

MEL, melamine; DCDA, dicyandiamide; TU, thiourea; ZNH, zinc nitrate hexahydrate; MB, methylene blue; MV, methyl violet; RhB, rhodamine B; RB, Rose Bengal; CV, crystal violet; MO, methyl orange; XO, xylenol orange; PR, phenol red; NA, not applicable.

3.6 Plausible Mechanism of Photocatalytic Degradation of Dyes

A plausible mechanism for the photocatalytic degradation of cationic MG and anionic CR dyes is presented in Fig. 7. Upon sunlight irradiation, the photocatalysts g-C_3N_4 and ZnO-NRs dispersed in the dye solution efficiently absorb photons at their surfaces. As a result, electrons are excited from the valence band (VB) to the conduction band (CB), leading to the generation of photogenerated electrons (e^-) in the CB and corresponding holes (h^+) in the VB of each photocatalyst [58,59,60,61].

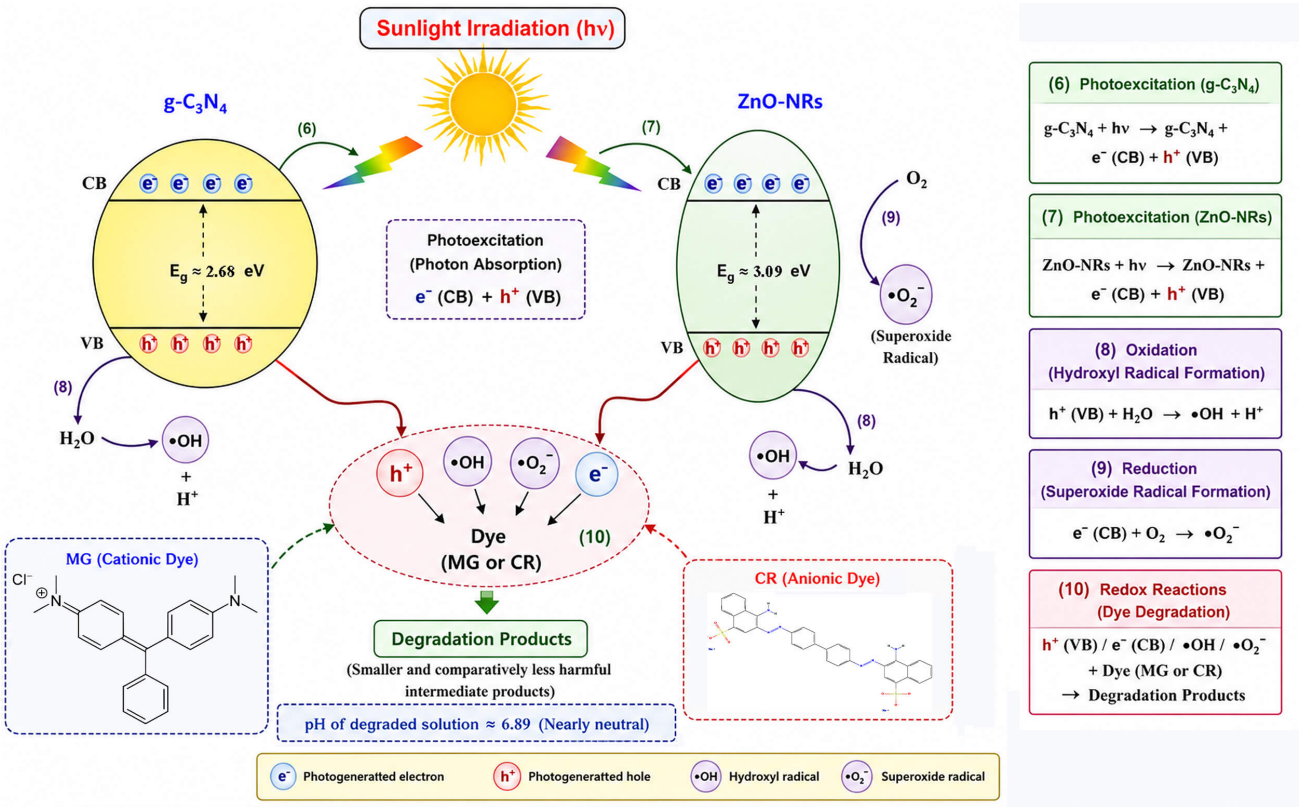


Fig. 7. Schematic illustration of sunlight-driven photocatalytic degradation of MG and CR mediated by g-C_3N_4 and ZnO-NRs.

Photoexcitation:

$$g\text{-}C_3N_4 + hv(Photon\ Absorption) \rightarrow g\text{-}C_3N_4 + e^-(CB) + h^+(VB) \quad (6)$$

$$ZnO\text{-}NRs + hv(Photon\ Absorption) \rightarrow ZnO\text{-}NRs + e^-(CB) + h^+(VB) \quad (7)$$

Oxidation (Hydroxyl Radical Formation):

$$h^+(VB) + H_2O \rightarrow \bullet OH + H^+ \quad (8)$$

Reduction (Superoxide Radicals):

$$e^-(CB) + O_2 \rightarrow \bullet O_2^- \quad (9)$$

Redox Reactions (Dye degradation):

$$h^+(VB)/e^-(CB)/\bullet OH/\bullet O_2^- + Dye(MG\ or\ CR) \rightarrow Degradation\ Products \quad (10)$$

The photogenerated holes either directly oxidize the dye molecules or react with water molecules adsorbed on the photocatalyst surface to produce highly reactive hydroxyl radicals (•OH). Simultaneously, the photogenerated electrons in the CB are captured by dissolved molecular oxygen (O_2), resulting in the formation of superoxide radicals ($\bullet O_2^-$) as illustrated in Eqns. 6,7,8,9,10. These reactive oxygen species play a crucial role in the oxidative degradation of MG and CR dyes into smaller and comparatively less harmful intermediate products. Moreover, the pH of the degraded dye solution was found to be nearly neutral (~6.89) after photocatalytic treatment. Therefore, the dominant reactive species involved in the degradation process could not be conclusively identified, and further investigations are required to validate the proposed reaction pathways.

4. Discussion

A comparative study of photocatalytic activities of the synthesized g-C_3N_4 and ZnO-NRs revealed that g-C_3N_4 exhibited better sunlight-mediated degradation performance against cationic MG and anionic CR dyes. The enhanced photocatalytic activity of g-C_3N_4 is mainly attributed to the narrower band gap energy and stronger visible-light absorption, resulting in enhanced photogenerated charge-carrier formation under sunlight exposure. Although ZnO-NRs demonstrate excellent crystallinity and well-defined rod-shaped morphology favorable for efficient

charge transport, their comparatively wider band gap makes them incapable of utilizing a sizable portion of the visible-light region of sunlight efficiently. On the contrary, the conjugated heptazine framework of g-C_3N_4 probably interacts more efficiently with aromatic dye molecules and enhances reactive oxygen species generation during photocatalysis.

Notably, substantial degradation of the anionic dye CR was observed even on a negatively charged catalyst surface, indicating that photocatalytic oxidation is not solely governed by electrostatic interactions but also proceeds via free-radical mechanisms involving reactive oxygen species, particularly hydroxyl (•OH) and superoxide ($\bullet O_2^-$) radicals generated under sunlight exposure.

The relatively shorter half-life values (i.e., higher degradation rate constants) for g-C_3N_4 also substantiated the higher photocatalytic efficiency. Moreover, the detection of intermediate degradation products through LC-MS analysis suggested that the dye molecules underwent progressive chemical decomposition into smaller molecules rather than simple decolorization.

In summary, the present study reveals that pristine g-C_3N_4, synthesized through a simple, environmentally friendly, and economically viable route, can function as an efficient visible-light-responsive photocatalyst for the degradation of organic pollutants under sunlight irradiation.

Limitations

The present study was conducted under controlled laboratory conditions using model dye pollutant degradation experiments, which may not fully reflect the potential of the synthesized g-C_3N_4 and ZnO-NRs photocatalysts under real environmental or industrial wastewater treatment conditions. Therefore, their applicability to complex wastewater containing mixed contaminants requires further investigation.

Although LC-MS analysis was employed to identify degradation intermediates, complete mineralization and systematic toxicity evaluation of the resulting by-products were not thoroughly investigated. In addition, advanced *in situ* investigations to directly monitor charge-transfer dynamics and surface reaction pathways during photocatalysis should be further explored. The recyclability and long-term operational stability of the photocatalysts under continuous flow conditions also require further evaluation.

Despite these limitations, the developed photocatalytic system demonstrates potential for sustainable wastewater treatment and aligns with the objective of SDGs: 6-Clean Water and Sanitation, 7-Affordable and Clean Energy, and 12-Responsible Consumption and Production. Future studies should therefore focus on real wastewater applications, long-term stability assessment, toxicity evaluation, and scale-up feasibility to validate its practical environmental application.

5. Conclusion

Herein, this study presents a comparative evaluation of the photocatalytic performance of g-C_3N_4 and ZnO-NRs for the degradation of cationic MG and anionic CR dyes under sunlight irradiation. Both photocatalysts demonstrated appreciable dye DEs; however, g-C_3N_4 consistently outperformed ZnO-NRs, achieving DEs of 90.21% for MG and 89.26% for CR within 150 min, compared to 66.78% and 63.75%, respectively, for ZnO-NRs. The enhanced photocatalytic activity of g-C_3N_4 is primarily attributed to its narrower band gap energy, improved visible light absorption capability, layered conjugated structure, and efficient generation of reactive oxygen species under sunlight irradiation. Moreover, the favorable interaction between the conjugated heptazine framework of g-C_3N_4 and dye molecules may also facilitate enhanced DE. The kinetic analysis further confirmed the superior photocatalytic efficiency of g-C_3N_4, exhibiting approximately 1.35–1.40 times higher degradation activity than ZnO-NRs for both cationic and anionic dyes. Moreover, LC-MS analysis of degraded dye solution confirmed the formation of intermediate degradation products, indicating the progressive photocatalytic decomposition of dye molecules. These findings demonstrate that g-C_3N_4 is a promising visible-light-active photocatalyst for the efficient degradation of organic pollutants and may offer potential applications in sunlight-driven wastewater remediation technologies.

Availability of Data and Materials

The data supporting the findings of this study are available from the corresponding authors upon reasonable request.

Author Contributions

S: Methodology, synthesis, analysis, testing, validation, investigation, and writing of the initial draft; SG: Formal analysis, resources, data curation, and review and editing of the original draft; MSA: Supervision, conceptualization, methodology, data curation, formal analysis, review and editing of the original draft, and manuscript rewriting; H: Formal analysis, resources, data curation, review and editing of the original draft, and figure improvement; AI: Resources, data curation, reference checking, and manuscript corrections; RKG: Resources, data curation, reference checking, and review and editing of the original draft; QIR: Supervision, conceptualization, methodology, data curation, formal analysis, review and editing of the original draft, and manuscript rewriting. All authors read and approved the final manuscript. All authors have participated sufficiently in the work and agreed to be accountable for all aspects of the work.

Ethics Approval and Consent to Participate

Not applicable.

Acknowledgment

The authors acknowledge the Integral Referral Laboratory, CIF, ICEIR, and Development section.

Funding

The study is funded by the Research Institute/Center Supporting Program (RICSP-26-1), King Saud University, Riyadh, Saudi Arabia.

Conflicts of Interest

The authors declare no conflicts of interest. M Shaheer Akhtar is serving as one of the Editorial Board members of this journal. We declare that M Shaheer Akhtar had no involvement in the peer review of this article and has no access to information regarding its peer review. Full responsibility for the editorial process for this article was delegated to Carmen-Georgeta Ristoscu.

Supplementary Material

Supplementary material associated with this article can be found, in the online version, at https://doi.org/10.31083/DJNB53465.

References

[1] Biswas A, Sarkar S, Das S, Dutta S, Choudhury MR, Giri A, et al. Water scarcity: A global hindrance to sustainable development and agricultural production - A critical review of the impacts and adaptation strategies. Cambridge Prisms: Water. 2025; 3: e4. https://doi.org/10.1017/wat.2024.16

[2] Lellis B, Fávaro-Polonio CZ, Pamphile JA, Polonio JC. Effects of textile dyes on health and the environment, and bioremediation potential of living organisms. Biotechnology Research and Innovation. 2019; 3: 275–290. https://doi.org/10.1016/j.biori.2019.09.001

[3] Dutta S, Adhikary S, Bhattacharya S, Roy D, Chatterjee S, Chakraborty A, et al. Contamination of textile dyes in aquatic environment: Adverse impacts on aquatic ecosystem and human health, and its management using bioremediation. Journal of Environmental Management. 2024; 353: 120103. https://doi.org/10.1016/j.jenvman.2024.120103

[4] Raghav S, Mansi G, Rajput YB, Prasad R, Jain P, Chavda V, et al. Recent advances in COF-based strategies for dye pollution remediation: Materials design, mechanistic insight, and future outlook. Separation and Purification Technology. 2025; 379: 134816. https://doi.org/10.1016/j.seppur.2025.134816

[5] Dutta S, Gupta B, Srivastava SK, Gupta AK. Recent advances on the removal of dyes from wastewater using various adsorbents: A critical review. Materials Advances. 2021; 2: 4497–4531. https://doi.org/10.1039/D1MA00354B

[6] Islam MT, Al Mamun MA, Halim AFMF, Peila R, Sanchez Ramirez DO. Current trends in textile wastewater treatment-bibliometric review. Environmental Science and Pollution Research International. 2024; 31: 19166–19184. https://doi.org/10.1007/s11356-024-32454-3

[7] Al-Tohamy R, Ali SS, Li F, Okasha KM, Mahmoud YAG, Elsamahy T, et al. A critical review on the treatment of dye-containing wastewater: Ecotoxicological and health concerns of textile dyes and possible remediation approaches for environmental safety. Ecotoxicology and Environmental Safety. 2022; 231: 113160. https://doi.org/10.1016/j.ecoenv.2021.113160

[8] Rathi BS, Kumar PS, Vo DVN. Critical review on hazardous pollutants in water environment: Occurrence, monitoring, fate, removal technologies and risk assessment. The Science of the Total Environment. 2021; 797: 149134. https://doi.org/10.1016/j.scitotenv.2021.149134

[9] Islam T, Repon MR, Islam T, Sarwar Z, Rahman MM. Impact of textile dyes on health and ecosystem: a review of structure, causes, and potential solutions. Environmental Science and Pollution Research International. 2023; 30: 9207–9242. https://doi.org/10.1007/s11356-022-24398-3

[10] Zakir O, Ait-Karra A, Khardazi S, Idouhli R, Khadiri ME, Dikici B, et al. Recent progress in nanomaterials for water treatment: A comprehensive review of adsorption, photocatalytic, and antibacterial applications. Journal of Water Process Engineering. 2025; 72: 107566. https://doi.org/10.1016/j.jwpe.2025.107566

[11] Shindhal T, Rakholiya P, Varjani S, Pandey A, Ngo HH, Guo W, et al. A critical review on advances in the practices and perspectives for the treatment of dye industry wastewater. Bioengineered. 2021; 12: 70–87. https://doi.org/10.1080/21655979.2020.1863034

[12] Fahad A, Darwish M, Ethaib S, Aris A, Ali IM, Ali N, et al. Innovative approaches to textile wastewater treatment: State-of-the-art technologies and future horizons. Scientific African. 2026; 32: e03341. https://doi.org/10.1016/j.sciaf.2026.e03341

[13] Chauke NM, Ngqalakwezi A, Raphulu M. Transformative advancements in visible-light-activated titanium dioxide for industrial wastewater remediation. International Journal of Environmental Science and Technology. 2025; 22: 8521–8552. https://doi.org/10.1007/s13762-025-06397-2

[14] Al-Nuaim MA, Alwasiti AA, Shnain ZY. The photocatalytic process in the treatment of polluted water. Chemicke Zvesti. 2023; 77: 677–701. https://doi.org/10.1007/s11696-022-02468-7

[15] Low J, Yu J, Jaroniec M, Wageh S, Al-Ghamdi AA. Heterojunction Photocatalysts. Advanced Materials (Deerfield Beach, Fla.). 2017; 29: 10.1002/adma.201601694. https://doi.org/10.1002/adma.201601694

[16] Al Miad A, Saikat SP, Alam MK, Sahadat Hossain M, Bahadur NM, Ahmed S. Metal oxide-based photocatalysts for the efficient degradation of organic pollutants for a sustainable environment: a review. Nanoscale Advances. 2024; 6: 4781–4803. https://doi.org/10.1039/d4na00517a

[17] Sharma S, Bassi A, Sanchita, Hasan I. Photocatalytic nanostructured materials for heavy metal remediation: Mechanisms, challenges, and future prospects. Materials Science in Semiconductor Processing. 2026; 204: 110269. https://doi.org/10.1016/j.mssp.2025.110269

[18] Ngulube KF, Abdelhaleem A, Osman AI, Peng L, Nasr M. Advancing sustainable water treatment strategies: harnessing magnetite-based photocatalysts and techno-economic analysis for enhanced wastewater management in the context of SDGs. Environmental Science and Pollution Research International. 2025; 32: 28159–28195. https://doi.org/10.1007/s11356-024-32680-9

[19] Hák T, Janoušková S, Moldan B. Sustainable Development Goals: A need for relevant indicators. Ecological Indicators. 2016; 60: 565–573. https://doi.org/10.1016/j.ecolind.2015.08.003

[20] Dong T, Cheung HYM, Man JHK, Zheng Z, Lo IMC. Recent advances in oxidant-involved photoelectrochemical systems for sustainable wastewater treatment: Mechanisms, applications, and perspectives. npj Materials Sustainability. 2025; 3: 41. https://doi.org/10.1038/s44296-025-00084-6

[21] Li X, Yu J, Jaroniec M. Hierarchical photocatalysts. Chemical Society Reviews. 2016; 45: 2603–2636. https://doi.org/10.1039/c5cs00838g

[22] Zhao Z, Sun Y, Dong F. Graphitic carbon nitride based

nanocomposites: a review. Nanoscale. 2015; 7: 15–37. https://doi.org/10.1039/c4nr03008g
[23] Kumar SG, Rao KK. Zinc oxide based photocatalysis: Tailoring surface-bulk structure and related interfacial charge carrier dynamics for better environmental applications. RSC Advances. 2015; 5: 3306–3351. https://doi.org/10.1039/C4RA13299H
[24] Yang L, Peng Y, Luo X, Dan Y, Ye J, Zhou Y, et al. Beyond C_3N_4 π-conjugated metal-free polymeric semiconductors for photocatalytic chemical transformations. Chemical Society Reviews. 2021; 50: 2147–2172. https://doi.org/10.1039/d0cs00445f
[25] Kumar SG, Kavitha R, Manjunatha C. Review and perspective on rational design and interface engineering of g-C3N4/ZnO: From type-II to step-scheme heterojunctions for photocatalytic applications. Energy & Fuels. 2023; 37: 14421–14472. https://doi.org/10.1021/acs.energyfuels.3c01032
[26] Liu AY, Cohen ML. Prediction of new low compressibility solids. Science (New York, N.Y.). 1989; 245: 841–842. https://doi.org/10.1126/science.245.4920.841
[27] Yu Y, Wang J. Direct microwave synthesis of graphitic C3N4 with improved visible-light photocatalytic activity. Ceramics International. 2016; 42: 4063–4071. https://doi.org/10.1016/j.ceramint.2015.11.078
[28] Ke P, Zeng D, Cui J, Li X, Chen Y. Improvement in structure and visible light catalytic performance of g-C3N4 fabricated at a higher temperature. Catalysts. 2022; 12: 247. https://doi.org/10.3390/catal12030247
[29] Narkbuakaew T, Sujaridworakun P. Synthesis of tri-s-triazine based g-C3N4 photocatalyst for cationic rhodamine B degradation under visible light. Topics in Catalysis. 2020; 63: 1086–1096. https://doi.org/10.1007/s11244-020-01375-z
[30] Khan MA, Mutahir S, Shaheen I, Qunhui Y, Bououdina M, Humayun M. Recent advances over the doped g-C3N4 in photocatalysis: A review. Coordination Chemistry Reviews. 2025; 522: 216227. https://doi.org/10.1016/j.ccr.2024.216227
[31] Imran M, Abdullah AZ, Rashid MS, Bakather OY, Alshoaibi AM, Khan ME, et al. Controlled morphology of g-C3N4 /metal oxide-based nanostructures applications in organic pollutant photodegradation: A review. Inorganic Chemistry Communications. 2026; 183: 115681. https://doi.org/10.1016/j.inoche.2025.115681
[32] Güell F, Galdámez-Martínez A, Martínez-Alanisa PR, Catto AC, da Silva LF, Mastelaro VR, et al. ZnO-based nanomaterials approach for photocatalytic and sensing applications: Recent progress and trends. Materials Advances. 2023; 4: 3685–3707. https://doi.org/10.1039/D3MA00227F
[33] Raha S, Ahmaruzzaman M. ZnO nanostructured materials and their potential applications: progress, challenges and perspectives. Nanoscale Advances. 2022; 4: 1868–1925. https://doi.org/10.1039/d1na00880c
[34] Rahman QI, Ahmad M, Misra SK, Lohani M. Effective photocatalytic degradation of rhodamine B dye by ZnO nanoparticles. Materials Letters. 2013; 91: 170–174. https://doi.org/10.1016/j.matlet.2012.09.044
[35] Ansari SN, Kavish M, Wagay JA, Khan Z, Khan AR, Ahmed S, et al. Sustainable synthesis of ZnO nanostructures using Ficus religiosa leaf extract with enhanced photocatalytic and antibacterial activity. Materials Science and Engineering: B. 2024; 310: 117752. https://doi.org/10.1016/j.mseb.2024.117752
[36] Wahab R, Ansari SG, Kim YS, Song M, Shin H. The role of pH variation on the growth of zinc oxide nanostructures. Applied Surface Science. 2009; 255: 4891–4896. https://doi.org/10.1016/j.apsusc.2008.12.037
[37] Aminuzzaman M, Ying LP, Goh WS, Watanabe A. Green synthesis of zinc oxide nanoparticles using aqueous extract of Garcinia mangostana fruit pericarp and their photocatalytic activity. Bulletin of Materials Science. 2018; 41: 50. https://doi.org/10.1007/s12034-018-1568-4
[38] Aminuzzaman M, Ng PS, Goh WS, Ogawa S, Watanabe A. Value-adding to dragon fruit (Hylocereus polyrhizus) peel biowaste: green synthesis of ZnO nanoparticles and their characterization. Inorganic and Nano-Metal Chemistry. 2019; 49: 401–411. https://doi.org/10.1080/24701556.2019.1661464
[39] Zhang J, Chen Y, Wang X. Two-dimensional covalent carbon nitride nanosheets: Synthesis, functionalization, and applications. Energy & Environmental Science. 2015; 8: 3092–3108. https://doi.org/10.1039/C5EE01895A
[40] Landi S Jr, Segundo IR, Freitas E, Vasilevskiy M, Carneiro J, Tavares CJ. Use and misuse of the Kubelka-Munk function to obtain the band gap energy from diffuse reflectance measurements. Solid State Communications. 2022; 341: 114573. https://doi.org/10.1016/j.ssc.2021.114573
[41] Ansari N, Ali A, Akhtar MS, Hasan S, Khatoon T, Khan AR, et al. Green synthesis of zinc oxide marigold shaped clusters using Eucalyptus globulus leaf extract as robust photocatalyst for dyes degradation under sunlight. Materials Science in Semiconductor Processing. 2024; 173: 108087. https://doi.org/10.1016/j.mssp.2023.108087
[42] Hasan S, Khan MA, Bano D, Iqbal A, Imran A, Rahman QI. Evaluation of physiochemical properties of g-C3N4/ZnO composites with enhanced photocatalytic activity under sunlight irradiation. Materials Science and Engineering: B. 2026; 324: 119008. https://doi.org/10.1016/j.mseb.2025.119008
[43] Sharma D, Saini A, Choudhary D, Kumari M, Chaudhary A, Dhayal V. In-situ synthesis of ZnO modified g-C3N4 composite: A potential photocatalyst and adsorbent for wastewater remediation. Materials Research Innovations. 2022; 26: 65–75. https://doi.org/10.1080/14328917.2021.1901424
[44] Gao J, Wang Y, Zhou S, Lin W, Kong Y. A facile one-step synthesis of Fe-doped g-C3N4 nanosheets and their improved visible-light photocatalytic performance. ChemCatChem. 2017; 9: 1708–1715. https://doi.org/10.1002/cctc.201700492
[45] Liu J, Zhang T, Wang Z, Dawson G, Chen W. Simple pyrolysis of urea into graphitic carbon nitride with recyclable adsorption and photocatalytic activity. Journal of Materials Chemistry. 2011; 21: 14398–14401. https://doi.org/10.1039/C1JM12620B
[46] Paul DR, Sharma R, Nehra SP, Sharma A. Effect of calcination temperature, pH and catalyst loading on photodegradation efficiency of urea derived graphitic carbon nitride towards methylene blue dye solution. RSC Advances. 2019; 9: 15381–15391. https://doi.org/10.1039/c9ra02201e
[47] Rattan Paul D, Nehra SP. Graphitic carbon nitride: a sustainable photocatalyst for organic pollutant degradation and antibacterial applications. Environmental Science and Pollution Research International. 2021; 28: 3888–3896. https://doi.org/10.1007/s11356-020-09432-6
[48] Mamba FB, Mbuli BS, Ramontja J. Synergistic effect of ZnO/Ag_2O@g-C_3N_4 based nanocomposites embedded in carrageenan matrix for dye degradation in water. Heliyon. 2024; 10: e31109. https://doi.org/10.1016/j.heliyon.2024.e31109
[49] Qiu S, Li J. High-Efficiency Ag-Modified ZnO/g-C_3N_4 Photocatalyst with 1D-0D-2D Morphology for Methylene Blue Degradation. Molecules (Basel, Switzerland). 2024; 29: 2182. https://doi.org/10.3390/molecules29102182
[50] Yadav AA, Kang S, Hunge YM. Photocatalytic degradation of Rhodamine B using graphitic carbon nitride photocatalyst. Journal of Materials Science: Materials in Electronics. 2021; 32: 15577–15585. https://doi.org/10.1007/s10854-021-06106-y
[51] Guan K, Li J, Lei W, Wang H, Tong Z, Jia Q, et al. Synthesis of sulfur doped g-C3N4 with enhanced photocatalytic activity in molten salt. Journal of Materiomics. 2021; 7: 1131–1142. https://doi.org/10.1016/j.jmat.2021.01.008

[52] Kadam AN, Kim H, Lee SW. Low-temperature in situ fabrication of porous S-doped g-C3N4 nanosheets using gaseous-bubble template for enhanced visible-light photocatalysis. Ceramics International. 2020; 46: 28481–28489. https://doi.org/10.1016/j.ceramint.2020.08.005

[53] Kumar MA, Ravikumar CR, Nagaswarupa HP, Purshotam B, Gonfa B, Murthy HA, et al. Evaluation of bi-functional applications of ZnO nanoparticles prepared by green and chemical methods. Journal of Environmental Chemical Engineering. 2019; 7: 103468. https://doi.org/10.1016/j.jece.2019.103468

[54] Ong CB, Mohammad AW, Rohani R, Ba-Abbad MM, Hairom NH. Solar photocatalytic degradation of hazardous Congo red using low-temperature synthesis of zinc oxide nanoparticles. Process Safety and Environmental Protection. 2016; 104: 549–557. https://doi.org/10.1016/j.psep.2016.04.006

[55] Vidya C, Prabha MC, Raj MA. Green mediated synthesis of zinc oxide nanoparticles for the photocatalytic degradation of Rose Bengal dye. Environmental Nanotechnology, Monitoring & Management. 2016; 6: 134–138. https://doi.org/10.1016/j.enmm.2016.09.004

[56] Rajendrachari S, Taslimi P, Karaoglanli AC, Uzun O, Alp E, Jayaprakash GK. Photocatalytic degradation of Rhodamine B (RhB) dye in wastewater and enzymatic inhibition study using cauliflower shaped ZnO nanoparticles synthesized by a novel one-pot green synthesis method. Arabian Journal of Chemistry. 2021; 14: 103180. https://doi.org/10.1016/j.arabjc.2021.103180

[57] Sadollahkhani A, Kazeminezhad I, Lu J, Nur O, Hultman L, Willander M. Synthesis, structural characterization and photocatalytic application of ZnO@ZnS core-shell nanoparticles. RSC Advances. 2014; 4: 36940–36950. https://doi.org/10.1039/C4RA05247A

[58] Hoffmann MR, Martin ST, Choi W, Bahnemann DW. Environmental applications of semiconductor photocatalysis. Chemical Reviews. 1995; 95: 69–96. https://doi.org/10.1021/cr00033a004

[59] Nosaka Y, Nosaka AY. Generation and Detection of Reactive Oxygen Species in Photocatalysis. Chemical Reviews. 2017; 117: 11302–11336. https://doi.org/10.1021/acs.chemrev.7b00161

[60] Wahba MA. Recent developments in metal oxide semiconductor photocatalysts for solar-driven environmental applications. Discover Materials. 2026; 6: 127. https://doi.org/10.1007/s43939-026-00585-8

[61] Tofil HM, Ghazi R, Ghaib FA, Dara RN, Kebaili I, Boukhris I, et al. Modified g-C3N4 photocatalysts for clean energy and environmental applications: A review. Sustainable Energy & Fuels. 2025; 9: 2900–2927. https://doi.org/10.1039/D4SE01620C